Measuring sea ice concentration in the Arctic Ocean using SMOS

Carolina Gabarro[1], Antonio Turiel[1], Pedro Elosegui[1,2], Joaquim A. Pla-Resina[1], and Marcos Portabella[1]

[1]Barcelona Expert Center. Institute of Marine Sciences, ICM/CSIC, Passeig Maritim Barceloneta 39, Barcelona, Spain.
[2]Massachusetts Institute of Technology, Haystack Observatory, Westford, MA, USA.

Correspondence to: Carolina Gabarro (cgabarro@icm.csic.es)

Abstract.

We present a new method to estimate sea ice concentration in the Arctic Ocean using brightness temperature observations from the Soil Moisture Ocean Salinity (SMOS) satellite. The method, which employs a Maximum Likelihood Estimator (MLE), exploits the marked difference in radiative properties between sea ice and seawater, in particular when observed over the wide range of satellite viewing angles provided by SMOS. Observations at L-band frequencies such as those from SMOS (i.e., 1.4 GHz, or equivalently 21-cm wavelength) are advantageous for the remote sensing of sea ice because the atmosphere is virtually transparent at that frequency.

We find that sea ice concentration is well determined (correlations of about 0.75) when compared to estimates from other sensors such as the Special Sensor Microwave/Imager (SSM/I and SSMIS). We also find that the performance of the method decreases under thin sea ice conditions (ice thickness $\lesssim$0.6 m). This result is expected because thin ice is partially transparent at L-band thus causing sea ice concentration to be underestimated. We therefore argue that SMOS estimates can be complementary to estimates of ice concentration of both thick and thin sea ice from other satellite sensors such as the Advanced Microwave Scanning Radiometer (AMSR-E and AMSR-2) or SSMIS, enabling a synergistic monitoring of pan-Arctic sea ice conditions.

1 Introduction

The Arctic Ocean is under profound transformation. The rapid decline in Arctic sea ice extent and volume that is both observed and modeled (e.g., Comiso, 2012; Stroeve et al., 2012) may have become the key illustration of change in a warming planet, but change is widespread across the whole Arctic system (e.g., AMAP, 2012; IPCC, 2013; SEARCH, 2013). A retreating Arctic ice cover has a marked impact on regional and global climate, and vice versa, through a large number of feedback mechanisms and interactions with the climate system (e.g., Holland and Bitz, 2003; Cohen et al., 2014; Vihma, 2014).

The launch of the Soil Moisture and Ocean Salinity (SMOS) satellite, in 2009, marked the dawn of a new type of space-based microwave imaging sensor. Originally conceived to map geophysical parameters of both hydrological and oceanographic interest (e.g., Martin-Neira et al., 2002; Mecklenburg et al., 2009), SMOS is also making serious inroads in the cryospheric sciences (e.g., Kaleschke et al., 2010, 2012; Huntemann et al., 2014). Developed by the European Space Agency (ESA), SMOS single payload, called Microwave Imaging Radiometer using Aperture Synthesis (MIRAS), is an L-band (1.4 GHz, or 21-cm wavelength) passive interferometric radiometer that measures the electromagnetic radiation emitted by Earth's surface. The

observed brightness temperature (T_B) can be related to moisture content over the soil and to salinity over the ocean surface (Kerr et al., 2010; Font et al., 2013), as can be used to infer sea ice thickness (Kaleschke et al., 2012) and snow thickness (Maaß, 2013; Maaß et al., 2015).

Sea ice concentration (SIC), defined as the fraction of ice relative to the total area at a given ocean location, is often used to determine other important climate variables such as ice extent and ice volume. SIC has therefore been the target of satellite-based passive microwave sensors such as AMSR-2 and SSMIS and the Advanced Microwave Scanning Radiometer (AMSR-E and AMSR-2) since more than 30 years because the brightness temperature of sea ice and seawater are quite distinct. There exists a variety of algorithms to retrieve SIC from T_B observations tuned to those higher-frequency sensors, that is frequencies between 6–89 GHz (e.g., Cavalieri et al., 1984; Comiso, 1986; Ramseier, 1991; Smith, 1996; Markus and Cavalieri, 2000; Kaleschke et al., 2001; Shokr et al., 2008). Those algorithms present different advantages and drawbacks depending on frequency, spatial resolution, atmospheric effects, physical temperature, and others. See for example Ivanova et al. (2015) for a review of a sample of thirteen of those algorithms. Although some authors (e.g., Mills and Heygster, 2011a; Kaleschke et al., 2013) have recently explored the feasibility of SIC determination using an aircraft-mounted L-band radiometer, a method that extends satellite-based SIC retrievals down to L-band (i.e., SMOS) frequencies has been missing. We therefore set out to develop a new method, which we present here.

A significant difference between high-frequency and L-band microwave radiometry is that unlike the former, the ice penetration of the latter is non-negligible (Heygster et al., 2014) . In other words, ice is more transparent (i.e., optically thinner) at low than at high microwave frequencies. As a consequence, the brightness temperature measured by an L-band antenna is not only emitted by the topmost ice surface layer but by a larger range of deeper layers within the ice. Thanks to that increased penetration in sea ice (about 60 cm depending on ice conditions), the SMOS L-band radiometer is also sensitive to ice thickness (Kaleschke et al., 2012; Huntemann et al., 2014). In fact, ideally one would want to estimate both SIC and sea ice thickness simultaneously (e.g., Mills and Heygster, 2011a), what is left for a future work.

Wilheit (1978) analyzed the sensitivity of microwave emissivity of open seawater to a variety of geophysical variables such as atmospheric water vapor, sea surface temperature, wind speed, and salinity as function of frequency (Figure 1). The figure illustrates that L-band (1-2 GHz) observations are in a sweet spot, with the effect of all variables but salinity being minimal around SMOS frequency. The same authors also showed that the signature of multi-year (MY) and first-year (FY) ice overlap in the lower microwave frequencies, while this is not the case at higher frequencies.

We exploit some of SMOS key observational features in this study to develop a new method to estimate SIC. These include a spatial resolution of about 35-50 km, combination of acquisition modes involving dual and full polarization, continuous multiangle viewing between nadir and 65°, wide swath of about 1200 km, and 3-day revisit time at the equator but more frequently at the poles. In particular, the multiangle viewing capability of SMOS is a noteworthy feature; it means that the same location on the Earth's surface can be observed simultaneously from a continuous range of angles of incidence as the satellite overpasses it.

The new method we present in this paper uses SMOS brightness temperature T_B and a Maximum Likelihood Estimator (MLE) to obtain SIC maps in the Arctic Ocean. We describe SMOS data and a radiative transfer model for sea ice that allows

us to compute its emissivity, in Sections 2 and 3, respectively. We then introduce the concept of tie points and its sensitivity to different geophysical parameters to help with SIC retrievals via algorithmic inversion of SMOS data, in Section 4.1, 4.2, 4.3 and 4.4, and the MLE inversion algorithm, in Section 4.5. We then perform an accuracy assessment of SIC estimates using SMOS by comparing them to an independent SIC dataset in Section 5. We close with a discussion and conclusions, in Section 6.

2 Data

2.1 SMOS data from the Arctic Ocean

Since its launch in 2009, ESA has been generating brightness temperature full-polarization data products from SMOS. In this study, we focus on the official SMOS Level 1B (L1B) product version 504 data north of 60° N from 2014 to estimate SIC. (The analysis of the entire SMOS dataset, which continues to be growing, is left for future work). The L1B data contains the Fourier components of T_B at the antenna reference frame (Deimos, 2010), from which one can obtain temporal snapshots of the spatial distribution of T_B (i.e., an interferometric T_B image) by performing an inverse Fourier transform. The T_B data are geo-referenced at an Equal-Area Scalable Earth (EASE) Northern hemisphere grid (Brodzik and Knowles, 2002) of 25 km on the side. The estimated radiometric accuracy of individual T_B measurements from SMOS is $\sim$2 K at boresight, and can increase up to $\sim$4.5 K in the Extended Alias Free Field-of-View (Corbella et al., 2011). Proceeding from L1B data, though computationally more demanding than the more traditional L1C data products, has several benefits. For example, it allows one to change the antenna grid from the operational size of 128x128 pixels to 64x64 pixels. As shown by Talone et al. (2015), the smaller grid is optimal in that it helps mitigate some of the spatial correlations between measurements that are present in the larger grid.

We corrected the T_B data for a number of standard contributions such as geomagnetic and ionospheric rotation and atmospheric attenuation (Zine et al., 2008). The galactic reflection is not significant at high latitudes, and no correction is applied. We then filtered out outliers (defined as those estimates that deviate by more than 3-σ from the mean value, where σ is the radiometric accuracy at the given point in the antenna plane), and filtered out T_B estimates in regions of the field of view that are known to have low accuracy due to aliasing (Camps et al., 2005), Sun reflections, and Sun tails.

To lower the noise level, we averaged T_B measurements from both ascending and descending orbits over periods of 3 days, which thus define the time resolution of our SIC maps, over each grid cell, and also averaged acquisitions in incidence angle of 2° intervals. We used a cubic polynomial fit to interpolate T_B to locations that might otherwise not have T_B estimates over the full range of incidence angles.

2.2 OSI-SAF and other sea ice data products

We used SIC maps from the database (product version OSI-401a) of the Ocean and Sea Ice Satellite Application Facility (OSI SAF) of the European Organization for the Exploitation of Meteorological Satellites (EUMETSAT) for comparison.

These are computed from brightness temperature observations from SSMIS at 19 and 37 GHz, are corrected for atmospheric effects using forecasts from the European Center for Medium Range Weather Forecasts (ECMWF), use monthly dynamic tie points (see below), are available on polar Stereographic 10-km grid for both polar hemispheres, and include SIC uncertainty estimates (Tonboe et al., 2016). In this study, we used daily SIC maps in the Arctic Ocean from the OSI-SAF northern hemisphere products since 2014.

We also used SIC estimates from ice charts generated from various sensors by the National Ice Center (Fetterer and Fowler, 2009) to define the region that will be used to compute the 100% ice-tie points (see below).

3 Theoretical model of sea ice radiation at microwave wavelengths

The goal of this study is to develop a method that allows us to estimate Arctic sea ice concentration at SMOS electromagnetic frequency. Our approach will be to first describe the theoretical framework for the radiation emitted by sea ice in L-band. We will then describe a procedure that is robust when the values of the physical parameters of the model are unknown, which is often the case.

As we discussed in Section 1, passive radiometers measure brightness temperature T_B with different incidece angle at the antenna plane, which can be expressed as:

$$T_B = \Upsilon \left[T_{B_{SURF}} + T_{B_{ATM\_DN}} \right] + T_{B_{ATM\_UP}}, \tag{1}$$

where Υ is the atmosphere transmitivity, $T_{B_{SURF}}$ is the self-emitted radiation from the surface, $T_{B_{ATM\_DN}}$ is the downward-emitted atmospheric radiation that gets scattered by the terrain in the direction of the antenna, and $T_{B_{ATM\_UP}}$ is the self-emitted upward radiation from the atmosphere. Focussing into the surface emission, it is defined as:

$$T_{B_{SURF}}(\theta) = e_s(\theta) T, \tag{2}$$

where θ is the incidence angle relative to zenith angle, e_s the surface emissivity, and T the physical temperature of the radiation-emitting body layer. (Hereafter, we will use T_B to refer to surface emissivity, for simplicity).

To calculate e_s, we will assume a sea ice model consisting of horizontal layers of three media – air, snow, and thick ice. We will use the incoherent approach (i.e., conservation of energy, instead of wave field treatment in the coherent approach) and the radiative transfer equation (e.g., Burke et al., 1979) to compute the net emission from the third and second media (i.e., ice and snow, respectively) into the first medium (i.e., air). The approach is similar to that used by other authors (e.g., Mills and Heygster, 2011b; Maaß, 2013).

The emissivity e and reflectivity Γ of a layer are related by $e = (1 - \Gamma)$. The reflectivity (sometimes also called R) is the ratio of reflected and incident radiation at the media boundaries for each polarization, and can be calculated using Fresnel equations, which depend non-linearly on the dielectric constant of the layers and θ, the angle of incidence of an observation.

The frequency-dependent dielectric constant of a medium is a complex number defined as $\hat{\varepsilon}(f) = \varepsilon^{'}(f) + i\varepsilon^{''}(f)$, where the real part $\varepsilon^{'}$ is related to the electromagnetic energy that can be stored in the medium, and the imaginary part $\varepsilon^{''}$ is related to the energy dissipated within the medium , and f is frequency. Another important quantity is the refraction index n, which is also a complex value, and for nonmagnetic materials is $n = \sqrt{\hat{\varepsilon}}$ (e.g., Ulaby et al., 1986). Note that brightness temperature varies linearly with emissivity (Eq. 2), hence also with reflectivity. . The nonlinearity is an advantageous property for remote sensing that can be exploited by the multi-angle viewing capability of SMOS.

Figure 2 shows the dependence of brightness temperature with angle of incidence for seawater and sea ice, as well as that of ice overlaid by a dry snow layer (see Eq. 3 below), for nominal Arctic temperature and salinity values. (Specifically, temperature and salinity values used were after Maaß (2013); for seawater –1.8°C and 30 psu, respectively, and for sea ice –10°C and 8 psu.) Note that the T_B of seawater is significantly less than that of ice, and that the latter is slightly less than that of snow over ice. Also note the nonlinear dependence of T_B on incidence angle, the difference between horizontally (H) and vertically (V) polarized waves for all three models, and the higher larger variation with the incidence angle of H than that of V over ice and snow (e.g., Maaß et al., 2015).

We calculate the brighness temperature T_B of our three-layer, plane-parallel radiative transfer model (Eq. 3) by propagating to the surface the reflectivity computed at and through the ice-snow and snow-air media boundaries, and making a number of simplifying assumptions. Specifically, our model assumes (a) that the media are isothermal and (b) that the thickness of the ice layer is semi-infinite so that radiation from an underlying fourth layer (i.e., seawater) does not need to be considered.

These assumptions are realistic for the spontaneous emission of sea ice that is thicker than about 60 cm at the observing frequency of SMOS, as we discussed in Section 1, since the underlying seawater then makes no contribution to the overall emissivity. (But see below for the case of thin ice.)

To further simplify our approach, we will assume that the snow layer in the model consists of dry snow, which is typical of winter Arctic conditions. Because dry snow is a lossless medium at 1.4 GHz, that means that there will be no attenuation in the snow layer. However, dry snow still has an effect in emissivity that changes with the angle of incidence according to Snell's law. We make this simplifying assumption because water in a wet snow layer will cause attenuation and therefore increase the total emissivity, but it is rarely possible to obtain meaningful data on the amount of water in wet snow.

The brightness temperature of a thick-ice, dry-snow layered body that is measured at an angle of incidence θ with respect to the local vertical, polarization p, and observing frequency f can be simply calculated by propagating onto the surface the radiation that results from multiple reflections and refractions at the two media boundaries (i.e., ice-snow and snow-air) accounting for the infinite number of reflections between layers as (Burke et al., 1979):

$$T_B(\theta,p,f) = \left(\frac{1-\Gamma_{as}}{1-\Gamma_{as}\Gamma_{si}\exp^{-2\tau}}\right) \cdot \left[(1+\Gamma_{si}\exp^{-\tau})(1-\exp^{-\tau})T_{snow} + (1-\Gamma_{si})\exp^{-\tau}T_{ice}\right] + T_{sky}\Gamma_{as}, \quad (3)$$

where Γ_{as} and Γ_{si} are the reflectivity at the air-snow and snow-ice boundaries, respectively, and T_{snow} and T_{ice} are the physical temperature in the snow and ice layers, respectively. The term τ is the attenuation factor and is defined as $\tau = 2\alpha\sec\theta\, d$, where

α is the attenuation constant and d the depth of the snow layer. T_{sky} is the temperature of the cosmic background. The dependence of T_B on θ, p, and f is embedded in the expressions of Γ and τ.

The attenuation constant α of the middle layer, in the case of a low-loss medium ($\varepsilon^{''}/\varepsilon^{'} << 1$), can be expressed as:

$$\alpha = \frac{\pi f}{c} \frac{\varepsilon^{''}}{\sqrt{\varepsilon^{'}}} \tag{4}$$

where c the speed of light. The skin depth is defined as $\delta_s = 1/\alpha$ (m) and characterizes how deep an electromagnetic wave can penetrate into a conducting medium (e.g., Ulaby and Long, 2014).

The permittivity of dry snow is dependent on the snow density (Tiuri et al. (1984); Matzler (1996)). For a snow density of $\rho_s = 300\,g/cm^3$, the dry snow permittivity at L-band is equal to $\varepsilon_{snow} = 1.47$, with negligible imaginary dielectric constant. Therefore, the snow attenuation coefficient α_{snow} is considered zero at this frequency.

To compute the complex dielectric constant of sea ice ε_{ice} (which is needed to compute Γ_{si}), we use the classic empirical relationship by Vant et al. (1978). In this model, permittivity depends linearly on the ice brine volume V_b as,

$$\hat{\varepsilon}_{ice} = a_1 + a_2 V_{br} + i(a_3 + a_4 V_{br}) \tag{5}$$

where $V_{br} = 10\,V_b$, and the coefficients a_i can be obtained by linear interpolation to 1.4 GHz of the laboratory values from microwave measurements at 1 and 2 GHz (refer to Vant et al. (1978) for coefficient values).

The sea ice brine volume V_b, can be computed using Cox and Weeks (1983) as follows:

$$V_b = \frac{\rho S}{F_1(T) - \rho S\, F_2(T)} \tag{6}$$

where ρ, S, and T are sea ice density, salinity, and temperature, respectively. The F functions are cubic polynomials derived empirically, namely

$$F_j(T) = \sum_{i=0}^{3} a_{ij} T^i \tag{7}$$

where the values of the coefficient a_{ij} were given in Leppäranta and Manninen (1998) for ice temperatures between –2 °C and 0 °C, and for lower temperatures in Cox and Weeks (1983); see also Thomas and Dieckmann (2003).

We also calculate the theoretical emissivity e_s of a four-layer model using the procedure described above. The additional layer in this model is the seawater under sea ice , and we used the dielectric constant of seawater from Klein and Swift (1977). This layer did not need to be considered for the case of (optically) thick ice described above, but it becomes "visible" for the case of (optically) thin ice (i.e., thicknesses $\lesssim$60 cm, depending on the ice temperature and salinity). Because the emissivity of seawater is significantly less than that of sea ice (Figure 2), the net effect of reducing the sea ice thickness and starting to sense seawater, is an overall decrease in surface emissivity, hence of T_B (as illustrated in Figure 5), relative to emissivity of thick ice (Shokr and Sinha, 2015).

4 Methods

4.1 Definition of robust indices from brightness temperature

It is rarely possible to obtain the ancillary geophysical data such as sea ice temperature, salinity, and ice thickness that is required to estimate brightness temperature from the microwave remote sensing model described above. Therefore, making assumptions and approximations becomes critically important as discussed above. It is possible, however, to define a number of indices (resulting from a combination of brightness temperature observations that are less sensitive to the unknown physical parameters. For example, estimates of soil moisture or sea ice concentration from radiometric measurements are often derived by combining T_B measurements obtained from different polarizations, frequencies, and angles of incidence (Becker and Choudhury, 1988; Owe et al., 2001). Combinations of T_B measurements might result in lower sensitivity than that of original T_B to the exact physical conditions, but good enough to distinguish among conditions such as deletedwhen a phase changes , thus increasing robustness.

We will use two indices hereafter, the polarization difference (PD) index and the angular difference (AD) index. The PD index is defined as the difference between T_B measurements obtained at vertical T_{B_V} and horizontal T_{B_H} polarizations as

$$\mathrm{PD}(\theta) = T_{B_V}(\theta) - T_{B_H}(\theta). \tag{8}$$

The AD index is defined as the difference between two vertical polarization T_B measurements obtained at two different angles of incidence as

$$\mathrm{AD}(\theta) = T_{B_V}(\theta + \Delta\theta) - T_{B_V}(\theta). \tag{9}$$

Figures 3 and 4 show the variation of PD and AD for the thick-ice model with angle of incidence, respectively. In defining AD, we use vertical rather than horizontal polarization because identification of the three media is facilitated by the larger dynamic range and non-crossing signatures of the former (Figure 4).We choose $\Delta\theta = 35^\circ$ angle difference because this value represents a good compromise between sensitivity and accuracy in the case of SMOS (Camps et al., 2005) and, importantly, is also well supported by the wide range of satellite viewing angles that characterizes SMOS.

4.2 Calibration of sea ice concentration using tie points

Tie points are widely used for retrieving SIC with higher frequency radiometers, as well as in other fields such as photogrammetry (e.g., Khoshelham, 2009). In this study, we will use tie points as ground-truth estimates of sea ice concentration. In this context, tie points are reference values of the two radiometric end-members for ocean pixels in the Arctic, that is, pixels that are completely covered by sea ice (i.e., 100% ice concentration) and pixels of open water (i.e., 0% ice concentration). In this applications, tie points can therefore be viewed as SIC calibration points because their expected radiation can be unambiguously determined.

Figure 3 shows theoretical PD tie-point values for open water and sea ice, as well as ice with a snow layer. The values for an angle of incidence of 50° are marked by solid red circles. This angle represents a good compromise in PD contrast between

the two media and SMOS accuracy (Camps et al., 2005). The two bounding values are 62.9 K (seawater) and 26.8 K ice with snow cover . The large difference between tie-point values suggests that it is possible to estimate SIC at L-band.

Figure 4 shows theoretical AD tie-point values for difference in incidence angle $\Delta\theta = 35^\circ$ and angles of incidence up to $\theta = 30^\circ$ (which, per Eq. 9, represents the T_{B_V} difference between $\theta = 60^\circ$ and $\theta = 25^\circ$). The values for an angle of incidence of 25° are marked by solid red circles, for which the tie points are 51.8 K (seawater) and 8.6 K (ice with snow cover)(see also Table 1). Hereafter, AD and PD will be evaluated at the incidence angles indicated above.

Figure 5 shows that, according the discussed 4-layer radiative transfer model, T_B at nadir increases non-linearly as function of ice thickness up to the saturation value of ∼250 K, which is reached when ice becomes ∼70-cm thick. Notice that in the figure, T_B estimates start at an ice thickness of 5 cm because there is a discontinuity in the Burke model as the thickness of ice tends to zero (e.g., Kaleschke et al., 2010; Mills and Heygster, 2011a; Maaß, 2013; Kaleschke et al., 2013). Also shown in Figure 5, theoretical AD and PD values for the incidence angles indicated above, as described by our model. Compared with T_B, the total variation of both AD and PD with ice thickness are significantly smaller.

4.3 Sensitivity of estimates of sea ice concentration to surface emissivity changes

We now turn to calculate the sensitivity of SIC estimates to changes in surface emissivity due to variations in the physical properties of sea ice (i.e., salinity, temperature, thickness). We will work with SIC estimated derived from for the three parameters T_B, PD, and AD . This is done following a standard error propagation method (as also used in Comiso et al. (1997)). It is important to determine how changes in ice conditions affect SIC estimates through those three indices to try to minimize SIC errors obtained using SMOS.

Table 2 lists the sensitivities, according to our theoretical model, of the indices I ($I = T_B$, PD, or AD) to the geophysical variables of ice and seawater: physical temperature (i.e., $\delta I/\delta T$), salinity ($\delta I/\delta S$), and thickness ($\delta I/\delta d$) evaluated within the ranges of T_{water}=[2,15], S_{water}=[10,38], T_{ice}=[-20,-5], and S_{ice}=[2,12]. It should be noted that those sensitivities are calculated using the model in Section 3. In order to assess which index is less sensitive to changes in a given geophysical variable, we will calculate absolute sensitivities, defined as the sensitivities multiplied by the dynamic range of the measurements.

Knowing the value of the tie points of sea ice (SIC=100%) and seawater (SIC=0%), one can compute the average slopes of the SIC estimates to their corresponding parameters T_B, PD, and AD (i.e., $\delta SIC/\delta T_B$, $\delta SIC/\delta PD$ and $\delta SIC/\delta AD$). From data in Table 1, we obtain the average slopes as: $\delta SIC/\delta T_B = 0.65$, $\delta SIC/\delta PD = 2.32$, and $\delta SIC/\delta AD = 2.77$. These slopes can be used to propagate T_B, AD, and PD errors to errors in the SIC estimates.

We will assume reasonable values for the variability of the physical parameters on which our emissivity model depends on, namely T, S and d of ice (generically denoted by g), as follows: ΔT=5 K, ΔS=4 psu, and Δd=30 cm. Using the values in Table 2 and the slopes calculated above, one can finally compute the errors in SIC estimates associated to the geophysical variability of g when the index I is used to evaluate SIC following Eq (10).

$$\Delta SIC|_g = |\frac{\delta SIC}{\delta I}| \cdot |\frac{\delta I}{\delta g}| \cdot \Delta g \tag{10}$$

To evaluate the final impact of geophysical variability on the SIC evaluation using the index I, we compute the root-sum-squared (RSS) of the SIC uncertainties due to the geophysical parameters (Table 3). The table shows that AD is the most robust index to retrieve SIC, slightly better than PD, and significantly better than T_B, as T_B is highly sentitive to ice thickness variations. Even given the uncertainties in the theoretical physical model of ice, we consider the differences significant enough to focus on inversion algorithms using the PD and AD indices, and not T_B, as done by other authors (e.g., Mills and Heygster, 2011a)).

4.4 Comparison with empirical tie points

Following the theoretical analysis above, we now turn to evaluate its performance empirically. We therefore select several regions of interest in the Arctic Ocean where SIC has been determined to be either 0% or 100% by other sensors and methods. To identify such regions, we used SIC maps from OSI-SAF and from the National Ice Center. In particular, we selected the open seawater region between latitudes 55°–70° N and longitudes 20° W and 25° E, which comprises more than 2000 pixels in a typical SMOS image. For sea ice, we selected the multi-year (MY) ice region between latitudes 78°–83° N (the northernmost latitude observable by SMOS) and longitudes 75°–150° W, which comprises about 1000 pixels per SMOS image. We expect some (yet unquantified) level of uncertainty associated with the selection of the region to compute the 100% tie point for summer periods stemming from known errors in the summer SIC products by OSI-SAF (Tonboe et al., 2016).

We calculated SMOS brightness temperatures of these target regions to evaluate their potential as empirical tie points for seawater and sea ice. Starting with T_B, Figure 6 shows the temporal variation, in 2014, of the spatially averaged (median) T_B at nadir of the two geographic regions above. The values are consistent with the modeled values in Table 1. For the seawater region, the Figure shows that the brightness temperature is constant, at about 99 K, to within $\sim$2.5 K (one σ standard deviation) throughout the year. For the ice region, T_B is also stable during the non-summer months, but it drops by about 20 K during the summer season due to changes in surface emissivity associated with snow and ice melt and concurrent formation of meltwater ponds. The factor-two increase in formal error in summer relative to winter is also an indication of increased radiometric variability in surface conditions (as shown in Table 1).

Figure 7 shows that the temporal radiometric stability of the seawater region throughout 2014, and that of sea ice during the non-summer months, is also reflected in the AD and PD indices, as one would expect. This suggests that a different set of tie-points during winter and summer period could be beneficial for the quality of the SIC retrievals.

Figure 8 shows a 2-D scatter plot of AD and PD indices for the two regions above during the March 2014 (winter tie-point) and during July (summer tie-point). The index values associated with seawater and with ice group forming form two well-differentiated clusters, which implies that the two types of regions can be clearly segregated using these indices. This is also true for the summer tie-points even though in this case the dispersion is larger and values are closer to sea tie-points, as expected following Figure 7.

Table 1 lists the modeled (with snow and without) and observed TB, AD, and PD tie-point values for winter and summer 2014, and the standard deviation (σ) of the measurements . It is encouraging that most of the values are in agreement at about

2σ, despite underlying model assumptions such as uniform sea ice temperature and specular ocean surface. Another important result is that the observed SMOS data is closer to the model when snow is considered.

4.5 Retrieval of sea ice concentration

The brightness temperature of mixed pixels, that is, ocean pixels partially covered by sea ice, can be expressed as a linear combination of the brightness temperature of ice and seawater weighted by the percentage of each surface type (e.g., Comiso et al., 1997):

$$T_{B_{mixed}} = C\,T_{B_{ice}} + (1-C)\,T_{B_{water}} \tag{11}$$

where C is the fraction of ice present in a pixel, with $C = 1$ corresponds to 100% of ice and $C = 0$ to 0% of ice, or equivalently 100% of seawater. Since AD and PD (Eqs. 8-9) depend linearly on brightness temperature, Eq. (11) can be used to express both AD and PD.

There are several possible strategies to estimate sea ice concentration at a given pixel from the AD and PD values measured at that pixel. The simplest approach is to consider that the values of the tie points are good representatives of the values of AD and PD at the respective medium, i.e., seawater and sea ice, such that

$$\begin{aligned} \mathrm{AD} &\approx C\,\mathrm{AD}_{ice} + (1-C)\,\mathrm{AD}_{water} \\ \mathrm{PD} &\approx C\,\mathrm{PD}_{ice} + (1-C)\,\mathrm{PD}_{water} \end{aligned} \tag{12}$$

Concentration C can thus be retrieved from the value of either AD or PD by inverting the associated linear equation. In general, C can also be evaluated simultaneously with the AD and the PD observations by averaging the values obtained from both indices, as:

$$C = \frac{1}{2}\left[\frac{\mathrm{AD}-\mathrm{AD}_{water}}{\mathrm{AD}_{ice}-\mathrm{AD}_{water}} + \frac{\mathrm{PD}-\mathrm{PD}_{water}}{\mathrm{PD}_{ice}-\mathrm{PD}_{water}}\right]. \tag{13}$$

This is known as the Linear Estimation of SIC. However, this approach might be too simple, as the values of AD and PD on ice and seawater can have some non-negligible dispersion due to geophysical conditions and to radiometric noise.

In this paper, a new inversion algorithm to estimate C is presented, which considers that AD and PD have known distributions, and by combining the observations it is possible to infer the value of C that is statistically more probable, given those observations.

The distributions of the SMOS AD and PD are unimodal and symmetric (not shown), thus allowing to approximate them by Gaussians and considering the pure ice and pure sea measurements as independent. Therefore we can easily use a Maximum-Likelihood Estimation (MLE) approach. The MLE has many optimal properties in statistical inference such as (e.g., Myung, 2003) sufficiency (the complete information about the parameter of interest is contained in the MLE estimator), consistency (the true value of the parameter that generated the data is recovered asymptotically, i.e. for sufficiently large samples), efficiency

(asymptotically, it has the lowest-possible variance among all possible parameter estimates), and parameterization invariance (same MLE solution obtained independent of the parametrization used).

Assuming the linearity superposition of indices (Eqs. 12), it follows that the distributions ρ of AD and PD in a general ocean pixel can be expressed as:

$$\rho_{\mathrm{AD}} \sim \mathcal{N}\left(C\,\overline{\mathrm{AD}}_{ice} + (1-C)\,\overline{\mathrm{AD}}_{water}, \sqrt{C^2\,\sigma^2_{\mathrm{AD}_{ice}} + (1-C)^2\,\sigma^2_{\mathrm{AD}_{water}}}\right) \tag{14}$$

$$\rho_{\mathrm{PD}} \sim \mathcal{N}\left(C\,\overline{\mathrm{PD}}_{ice} + (1-C)\,\overline{\mathrm{PD}}_{water}, \sqrt{C^2\,\sigma^2_{\mathrm{PD}_{ice}} + (1-C)^2\,\sigma^2_{\mathrm{PD}_{water}}}\right) \tag{15}$$

where the bar over the AD and PD indices refers to their mean values, the subindex identifies the medium, and σ is the associated standard deviation for each index and media. To obtain the mean and standard deviation values, we used the SMOS measurements at the tie-point regions and periods discussed above (see Sect. 4.4). The symbol $\mathcal{N}$ means normal probability density function, that is:

$$f(x|\mu,\sigma) = \frac{1}{\sigma\sqrt{2\pi}}\cdot e^{-\frac{(x-\mu)^2}{2\sigma^2}} \tag{16}$$

As a first approximation, we will consider AD and PD two independent variables. It thus follows that the likelihood function $\mathcal{L}$ is equal to the product of their distributions or, equivalently and conveniently, to their sum (recall that the likelihood is the logarithm of the probability density function), thus:

$$\widehat{l} = \ln(\mathcal{L}) = \ln(\rho_{AD}) + \ln(\rho_{PD}) \tag{17}$$

The MLE of SIC is the value of C that maximizes the likelihood function $\widehat{l}$.

5 Results

5.1 Internal consistency of SMOS SIC retrievals

We have calculated AD and PD values from SMOS brightness temperature and used the MLE approach described above to obtain SIC estimates over the Arctic Ocean, in 2014. We have estimated SIC using different tie points, characterized by their central value and dispersion. For seawater , we have used a single, year-round median value and the associated standard deviation for each index. For ice tie points, we have used two sets of values, as suggested by the results in Figure 7. For the first set, we have computed for all years the median of the tie-points between December and May (see Table 1), i.e., the winter-spring months when Arctic sea ice extent is close to its annual maximum. For the second set, we used those same winter-spring values for the months of October through May but the average of the summer values for the months between June and September (see Table 1). We did not use the October nor November data to compute ice tie-points values because

these are replacedmoenthsepochs of maximum extension of thin ice, and underlying emission through thin ice could cause some errors on the SIC estimates (as shown in Figure 5 and Table 2).

Figure 9 shows the root-mean-square (RMS) error, relative to OSI-SAF, of SIC retrievals over the Arctic Ocean using four types of retrievals and two sets of tie-points . Introducing a specific set of summer tie-points (black plain line) reduces the RMS error with respect to using only one unique tie-point for the whole year (black dotted line). The RMS reduction is about 24% and 12% in July and August, respectively, and to smaller degree in June and September. Therefore, we will hereafter use a different set of tie-points values in summer and winter.

Furthermore, using the set of summer-winter tie-points leads to a significant reduction of the RMS error, relative to OSI-SAF, for four types of inversion methods, as shown in Figure 9. The figure shows the results of the four combinations of inversion methods namely linear and MLE, the set of indices that allow to discriminate SIC – either AD alone or AD and PD in combination. The lowest RMS values through all months in 2014 but January are obtained with the MLE inversion algorithm and the AD index alone. The evolution along the year of the RMS obtained with the linear retrieval method is similar in the case of the linear method, but at $\sim$5-10% increased noise level. Larger RMS values and increased temporal variability are observed when the PD index is also used. The RMS error of all retrievals is largest in Fall, in particular if the PD index is used. Those are months of ice formation, therefore vast regions become covered with frazil ice, nilas, and thin young ice, following the minimum ice extension of September. All methods converge to similar results in September, since this period is the one with minimum ice extension and minimum thin ice is expected (so resulting in very small difference between using AD or AD and PD methods). In the next subsection, a physical explanation and analysis of the behaviour during Fall is given.

Figure 10 shows the spatial variation of the difference in MLE SIC retrievals when using only the AD index and when using the AD and PD indices for the period 2–5 November 2014. As expected, the largest differences are associated with regions of thin ice formation, in particular in the Laptev Sea, Kara Sea, and along the edge of the ice pack both in the western Arctic and the Atlantic sector. Together, the spatio-temporal snapshots in Figures 9–10 highlight the sensitivity of PD to the presence of thin ice, what naturally leads to an increase of the retrieval error when PD is used. This conclusion is not fully consistent with the analysis done using the models in Section 4.3, on the dependence of the indices (T_B, PD, AD) on ice thickness. Table 2 shows that, theoretically, PD is slightly less sensitive to thin ice than AD. However, the AD index is the one less sensitive (lowest RSS) to variations of all the analysed variables. Therefore, we will hereafter use the AD index, summer-winter tie-points values, and an MLE-based estimator for SIC retrievals.

5.2 Accuracy assessment of SMOS SIC retrievals

As we have shown, we have evaluated the mutual consistency of the SMOS SIC retrievals, and in the process we have determined which is the approach that leads to the minimum error in the retrieval of SIC. We will now evaluate the accuracy of those retrievals. Although there does not exist a representative (in the space-time domain) ground-truth dataset that allows us to assess the accuracy of SMOS retrievals, the SIC estimates from OSI-SAF (already used above) are a good option because they are independent from SMOS, the spatio-temporal sampling and resolution of their products is commensurate with that of SMOS, and their error budget is available.

Figure 11 shows the spatial distribution of SIC in the Arctic Ocean estimated from (a) SMOS for the 3-day period 2–5 March 2015, (b) OSI-SAF SIC on 4 March 2014, and (c) the difference between (b) and (a). We have shown March because is the month of maximum sea ice extent, but the results for other months are similar. As explained, the largest differences between both algorithms are located at the margins of the sea ice cover, where thinner ice can be expected.

Figure 12 is the same as Figure 11 but here for some days in November, the month of maximum extension of thin young ice . Significant differences are now observed over a much wider area of the Arctic Ocean including the Barents, Kara, Laptev, East Siberian, and Beaufort seas. That is because thin ice is widely present in this season, and the radiometric response of SMOS to thin ice and the response of the microwave radiometers used by OSI-SAF are distinctly different.

That response is linked to the brightness temperature measured by a passive microwave radiometer, which increases with sea ice thickness up to a saturation value. Such an increase is more gradual for low frequencies and horizontal polarization (e.g., Ivanova et al., 2015). At the SMOS L-band, the increase of emissivity with ice thickness reaches saturation for an ice thickness that is about 60 cm, depending on ice salinity and temperature (Kaleschke et al., 2012) whereas at the OSI-SAF frequencies is only a few cm (Heygster et al., 2014; Ivanova et al., 2015). It is reasonable to infer that the observed SIC differences between SMOS and OSI-SAF are mainly associated with the different thickness of thin ice and ensuing penetration depths. For example, for pixels that are 100% covered by thin ice of say 25-cm thickness, the AD and PD values for these pixels will be slightly different than the tie-point value of ice because the value of ice tie point was computed from thick, MY ice (see Figure 5) for model analysis. This contrast leads to a difference in classification of such pixels, that will be considered mixtures of water and ice in the case of SMOS, and as 100% ice with OSI-SAF. In other words, the estimation of SIC of a seas covered by frazil ice and nilas will be higher for OSI-SAF than for SMOS.

To further analyze this classification difference, we calculated the probabilities of SMOS SIC conditioned by values of OSI-SAF SIC using a full year, 2014, of Arctic-wide estimates. Figure 13 shows (red) the probability of estimating a SIC value with SMOS that is less or equal than 5% when the estimated OSI-SAF SIC is 0%. As expected, the conditioned probability is very high throughout the year. This implies that both products have a similar ability to detect (close to) 100% ocean pixels. This implies that the probability of having high SMOS SIC values when OSI-SAF is low is almost zero, which also means that the rate of triggering false alarms on ice detection with SMOS is low.

Figure 13 also shows (blue) the opposite situation, that is the probability of estimating a SMOS SIC equal or higher than 90% while the OSI-SAF SIC is 100%. During the winter period (between January and April), the conditioned probability is notably high (near 0.90). Then it decreases sharply during spring and most notably in summer. The change in conditioned probability starting in the spring could stem from a change in ice properties as well as differences in the retrieval algorithm. Ice properties change because as the snow becomes wetter with the onset of the melt season in the spring, the observed emissivity starts to change. And regarding algorithms because OSI-SAF uses dynamically-adjusted tie points (every 30 days) while the SMOS algorithms introduced here use two tie-points (summer and winter), what would explain the decrease of the conditioned probability. The observed increase of the conditioned probability in June could be due to the use of summer tie-point (applied from June to September) which improve the RMS with respect OSISAF as shown in Figure 9. The low conditioned probability in Fall can be explained by the presence of thin ice, as described above.

Figures 14 map the spatial distribution of the conditioned probability of SIC estimates for the months of March (a) and November (b). In the figures, the Arctic Ocean has been color-coded in three regions whereby both products have SIC above 0.9 (red) , OSI-SAF SIC is more than 0.9 while SMOS SIC is less than 0.9 (light blue) and OSI-SAF and SMOS SIC is less than 0.9 (dark blue). It becomes apparent that the light blue regions outline the edge of the ice cover, what is in good correspondence with the expected areas of thin ice.

Figure 15 shows the monthly spatial coefficients of determination (that is, the square of the correlation coefficients) between SMOS and OSI-SAF SIC throughout 2014. Because the values of SIC tend to be either 0 or 1 over wide Arctic regions, we have excluded both extremes from the figure as this would lead to too high, non-significant values of correlation. Thus, we have only included SIC values between 0.05 (5%) and 0.95 (95%) when computing correlations. During the winter months, the determination coefficient is high (more than 0.65), what again is consistent with our interpretation about the role of thin ice in SMOS SIC (during winter thin ice is scarce and is present only at the edge of the ice cover). As melt starts, the correlation between SIC estimates continues to be high, thanks to the summer tie-point. In September, ice cover extent is at minimum but because ice growth has not started yet there is almost no thin ice, and the correlation remains high. The correlation drops in the Fall (between October and December) because ice growth starts by freezing of the sea surface, producing large amounts of new thin ice.

6 Discussion and Conclusions

According to Ivanova et al. (2015), the first source of error in the computation of sea ice concentration is the sensitivity to changes in the physical temperature of sea ice, in particular for those algorithms that use measurements between 10–37 GHz. The atmosphere has been identified as the second source of error, especially for the presence of water vapor and cloud liquid water but it is the first source of error for those algorithms which uses the 89GHz bands. Another problem faced by higher frequency radiometers is that the SIC retrievals are affected by the thickness of snow cover, which is difficult to determine.

However, the sensitivity of the brightness temperature to sea surface temperature, atmosphere, and wind speed is clearly reduced when observing the sea surface with radiometers working at lower frequencies (Figure 1), thus making SMOS more reliable and stable in those situations. Moreover, SMOS T_B is not affected by the snow thickness, as stated in Section 3.

Ivanova et al. (2015) states that the observed time trends in the measurements obtained by higher frequency radiometers are not only caused by trends in sea ice extent, but also by trends in the atmospheric and surface effects influencing the microwave emission measured by the satellite. Those authors observed seasonal changes on the ice tie-point of up to 10 K. In order to compensate those effects, they propose to dynamically derive the tie-points using a two-week running window; therefore, a new set of tie points is defined daily.

Figures 6 and 7 show that SMOS T_B, PD, and AD have low sensitivity to surface physical changes, and present small trend (for the year observed). Thanks to that, one can safely assume two sets of static (i.e., not temporally varying) tie-points (summer and winter) for SMOS data.

On the other hand, the best spatial resolution of SIC measurements with SMOS is about 35 km, which is low compared to the ∼3-km resolution that can be achieved with higher-frequency radiometers. Therefore, SMOS-based SIC estimates may be better suited for global climate studies. Another problem that the retrieval of SIC with SMOS has to deal with is the underestimation of SIC values when thin ice (less than ∼0.60 m) is present, which are characteristic for the ice edges and freeze-up periods.

Two indices derived from brightness temperatures, the Polarization Difference (PD) and the Angular Difference (AD), have been designed to maximize their differences between open water and sea ice. They have both low response to changes in the geophysical characteristics of the media, what has been confirmed by using theoretical models and sensitivity analysis.

Tie-points, defined as the characteristic values of our reference indices on the different media, have been calculated from SMOS data. When compared to the theoretical values derived from the model some small discrepancies (around 10-20%) have been observed, probably due to the simplifying assumptions (i.e flat surface ice, flat sea, constant temperature at the layers, etc.) used in theoretical models. We have thus decided to follow a more empirical approach. The use of two sets of tie points, one for summer and one for winter measurements, improves the results of the summer SIC maps relative to a static unique tie point. This improvement is not caused by changes in the ice or sea physical temperature, but most probably changes in the ice properties, because as snow and ice become wetter during the melt season, the observed radiometric emission change. This effect is also observed on measurements from radiometers at higher frequencies than SMOS.

We have introduced the MLE inversion algorithm to retrieve SIC from SMOS data. The method is based on the maximization of the a posteriori likelihood of the joint distribution of AD and PD, assuming that they are independent and Gaussianly distributed. This MLE algorithm is more robust (less noisy) than the linear inversion (Eq. 12). It also improves the retrieved SMOS SIC with respect to a linear inversion method because the former takes into account the dispersion (error) of the tie-points (reference), which makes the algorithm more robust to T_B errors. SIC maps obtained using only the AD index are of better quality than when the AD and PD indices are used together. We attribute this to the higher sensitivity of PD than AD to physical changes in the media, as shown here both theoretically and empirically.

The SMOS and OSI-SAF SIC maps compare well in terms of correlation (correlation coefficient higher than 0.65) and RMS except in areas of thin sea ice. This difference can be explained by the higher ice penetration of SMOS, of about 60 cm, relative to the penetration from higher frequency radiometers. Thus, when ice is thinner than 60 cm SMOS data lead to lower values of SIC, what has been verified in this study. These results suggest that by combining SIC information from SMOS and OSI-SAF, one could potentially develop a mask for locations of thin ice.

The study presented here can be expanded in a variety ways, which we are currently exploring. For example, one could improve the quality of SIC maps by using more tie-points and better characterizing them over different spatial regions and for various times of year. One could also attempt to simultaneously estimate SIC and ice thickness (e.g. Rothrock et al., 1988) over thin-ice regions by combining all the different SMOS observations acquired over the same point, thus providing independent estimates of ice volume over these regions. The study could also be further developed in the time-space domain since the present study has focused in a small fraction of the SMOS dataset making use of just four measurements from each pixel (two incidence angles and two polarizations), when more than 100 acquisitions can be obtained at each overpass.

Acknowledgements. This study has been funded by the National R+D Program of the Spanish Ministry of Economy through the Promises project ESP2015-67549-C3-R, as well as by previous SMOS-related grants.

References

AMAP: Changes in Arctic Snow, Water, Ice and Permafrost, Arctic Climate Issues 2011: Arctic Monitoring and Assessment Programme (AMAP), SWIPA 2011 Overview Report, Oslo, 2012.

Becker, F. and Choudhury, B. J.: Relative Sensitivity of Normalized Difference Vegetation Index (NDVI) and Microwave Polarization Difference Index (MPDI) for Vegetation and Desertification Monitoring, Remote Sens. Environ., 24, 297–311, 1988.

Brodzik, M. J. and Knowles, K. W.: EASE-Grid: A Versatile Set of Equal-Area Projections and Grids, Discrete Global Grids, 2002.

Burke, W., Schmugge, T., and Paris, J.: Comparison of 2.8- and 21-cm Microwave Radiometer Observations Over Soils With Emission Model Calculations, Journal of Geophysical Research, 84, 1979.

Camps, A., Vall-llossera, M., Duffo, N., Torres, F., and Corbella, I.: Performance of Sea Surface Salinity and Soil Moisture Retrieval Algorithms with Different Ancillary Data Sets in 2D L-band Aperture Synthesis Interferometic Radiometers, IEEE Transactions on Geoscience and Remote Sensing, 43, 1189–1200, doi:10.1109/TGRS.2004.842096, 2005.

Cavalieri, D., Gloersen, P., and Campbell, W.: Determination of sea ice parameters with the NIMBUS 7 SMMR, J. Geophys. Res., 89, 5355–5369, 1984.

Cohen, J., Screen, J. A., Furtado, J. C., Barlow, M., Whittleston, D., Coumou, D., Francis, J., Dethloff, K., Entekhabi, D., Overland, J., and Jones, J.: Recent Arctic amplification and extreme mid-latitude weather, Nature Geosci, 7, 627–637, doi:DOI: 10.1038/NGEO2234, 2014.

Comiso, J. C.: Characteristics of arctic winter sea ice from satellite multispectral microwave observations, J. Geophys. Res., 91, 975–994, 1986.

Comiso, J. C.: Large Decadal Decline of the Arctic Multiyear Ice Cover, Journal of Climate, 25, 1176–1193, doi:10.1175/JCLI-D-11-00113.1, 2012.

Comiso, J. C., Cavalieri, D. J., Parkinson, C. L., and Gloersen, P.: Passive microwave algorithms for sea ice concentration: A comparison of two techniques, Remote Sensing of Environment, 60, 357 – 384, doi:http://dx.doi.org/10.1016/S0034-4257(96)00220-9, 1997.

Corbella, I., Torres, F., Duffo, N., Gonzalez-Gambau, V., Pablos, M., Duran, I., and Martin-Neira, M.: MIRAS Calibration and Performance: Results From the SMOS In-Orbit Commissioning Phase, Geoscience and Remote Sensing, IEEE Transactions on, 49, 3147 –3155, doi:10.1109/TGRS.2010.2102769, 2011.

Cox, G. and Weeks, W.: Equations for Determining the Gas and Brine Volumes in Sea-Ice Samples, Journal of Glaciology, Vol. 29. No. 102, 1983.

Deimos: SMOS L1 Processor Algorithm Theoretical Baseline Definition, SO-DS-DME-L1PP-0011, Tech. rep., Deimos Engenharia, 2010.

Fetterer, F. and Fowler, C.: National Ice Center Arctic Sea Ice Charts and Climatologies in Gridded Format, Version 1, http://dx.doi.org/10.7265/N5X34VDB, 2009.

Font, J., Boutin, J., Reul, N., Spurgeon, P., Ballabrera-Poy, J., Chuprin, A., Gabarró, C., Gourrion, J., Guimbard, S., Hénocq, C., Lavender, S., Martin, N., Martínez, J., McCulloch, M., Meirold-Mautner, I., Mugerin, C., Petitcolin, F., Portabella, M., Sabia, R., Talone, M., Tenerelli, J., Turiel, A., Vergely, J., Waldteufel, P., Yin, X., Zine, S., and Delwart, S.: SMOS first data analysis for sea surface salinity determination, International Journal of Remote Sensing,, DOI:10.1080/01431161.2012.716541, 2013.

Heygster, G., Huntemann, M., Ivanova, N., Saldo, R., and Pedersen, L. T.: Response of passive microwave sea ice concentration algorithms to thin ice, in: 2014 IEEE Geoscience and Remote Sensing Symposium, pp. 3618–3621, doi:10.1109/IGARSS.2014.6947266, 2014.

Holland, M. M. and Bitz, C. M.: Polar amplification of climate change in coupled models, Climate Dynamics, 21, 221–232, doi:10.1007/s00382-003-0332-6, http://dx.doi.org/10.1007/s00382-003-0332-6, 2003.

Huntemann, M., Heygster, G., Kaleschke, L., Krumpen, T., Mäkynen, M., and Drusch, M.: Empirical sea ice thickness retrieval during the freeze up period from SMOS high incident angle observations, The Cryosphere, 7, 4379–4405, doi:doi:10.5194/tc-8-439-2014, 2014.

IPCC: Climate Change 2013: The Physical Science Basis, Fifth Assessement, Tech. rep., Cambridge University Press, 2013.

Ivanova, N., Pedersen, L. T., Tonboe, R. T., Kern, S., Heygster, G., Lavergne, T., Sørensen, A., Saldo, R., Dybkjær, G., Brucker, L., and Shokr, M.: Satellite passive microwave measurements of sea ice concentration: an optimal algorithm and challengesdoi:10.5194/tcd-9-1269-2015, The Cryosphere., 9, 1797–1817, doi:10.5194/tc-9-1797-2015, 2015.

Kaleschke, L., Lupkes, C., Vihma, T., Haarpaintner, J., Bochert, A., Hartmann, J., and Heygster: SSM/I Sea ice remote sensing for mesoscale ocean–atmosphere interaction analysis,, Canadian Journal of Remote Sensing, 27, 5, 526–537, 2001.

Kaleschke, L., Maaß, N., Haas, C., Hendricks, S., Heygster, G., and Tonboe, R. T.: A sea-ice thickness retrieval model for 1.4 GHz radiometry and application to airborne measurements over low salinity sea-ice,, The Cryosphere, doi:10.5194/tc-4-583-2010, 4, 583–592, 2010.

Kaleschke, L., Tian-Kunze, X., Maaß, N., Mäkynen, M., and Drusch, M.: Sea ice thickness retrieval from SMOS brightness temperatures during the Arctic freeze-up period, Geophys. Res. Lett., doi:10.1029/2012GL050916, 2012.

Kaleschke, L., Tian-Kunze, X., Maaß, N., Heygster, G., Huntemann, M., Wang, H., Hendricks, S., and Krumpen, T.: SMOS Sea Ice Retrieval Study (SMOSIce). Final Report, Tech. rep., ESA ESTEC Contract No.: 4000101476/10/NL/CT., http://icdc.zmaw.de/fileadmin/user_upload/icdc_Dokumente/SMOSICE_FinalReport_2013.pdf, 2013.

Kerr, Y., Waldteufel, P., Wigneron, J., Delwart, S., Cabot, F., Boutin, J., Escorihuela, M., Font, J., Reul, N., Gruhier, C., Juglea, S., Drinkwater, M., Hahne, A., Martin-Neira, M., and Mecklenburg, S.: The SMOS mission: New tool for monitoring key elements of the global water cycle, Proc. IGARSS 2010, no. 5., 98, 666–687, 2010.

Khoshelham, K.: Role of Tie Points in Integrated Sensor Orientation for Photogrammetric Map Compilation, Photogrammetric Engineering and Remote Sensing, 75, 305–311, doi:doi:10.14358/PERS.75.3.305, 2009.

Klein, L. and Swift, C.: An Improved Model for the Dielectric Constant of Sea Water at Microwave Frequencies, IEEE Transactions on Antennas and Propagation, AP-25, 104–111, 1977.

Leppäranta, M. and Manninen, T.: The brine and gas contents of sea-ice with attention to low salinities and high temperatures, Internal Report 2, Tech. rep., , Finnish Institute of Marine Research, 1998.

Maaß, N.: Remote Sensing of Sea Ice thickness Using SMOS data, Master's thesis, Hamburg University, 2013.

Maaß, N., Kaleschke, L., Tian-Kunze, X., and T., R.: Snow thickness retrieval from L-band brightness temperatures: a model comparison, Annals of Glaciology, 56(69), doi: 10.3189/2015AoG69A886, 2015.

Markus, T. and Cavalieri, D.: An enhancement of the NASA Team sea ice algorithm, IEEE T.Geosci. Remote, 38, 1387–1398, 2000.

Martin-Neira, M., Ribó, S., and Martin-Polegre, A. J.: Polarimetric mode of MIRAS, IEEE Transactions on Geoscience and Remote Sensing, 40, 1755–1768, doi:10.1109/TGRS.2002.802489, 2002.

Matzler, C.: Microwave permittivity of dry snow, IEEE Transactions on Geoscience and Remote Sensing, 34, 573–581, doi:10.1109/36.485133, 1996.

Mecklenburg, S., Wright, N., Bouzina, C., and Delwart, S.: Getting down to business - SMOS operations and products., ESA Bulletin, 137, 25–30, 2009.

Mills, P. and Heygster, G.: Retrieving Ice Concentration From SMOS, Geoscience and Remote Sensing Letters, IEEE, 8, 283–287, doi:10.1109/LGRS.2010.2064157, 2011a.

Mills, P. and Heygster, G.: Sea Ice Emissivity Modeling at L-Band and Application to 2007 Pol-Ice Campaign Field Data, IEEE Transactions on Geoscience and Remote Sensing, 49, 612–627, doi:10.1109/TGRS.2010.2060729, 2011b.

Myung, J.: Tutorial on maximum likelihood estimation, Journal of Mathematical Psychology, 47, 90–100, 2003.

Owe, M., Jeu, R., and Walker, J.: A Methodology for Surface Soil Moisture and Vegetation Optical Depth Retrieval Using the Microwave Polarization Difference Index, IEEE Transactions on Geoscience and Remote Sensing, 39, No. 8, 1643–1654, doi:10.1109/36.942542, 2001.

Ramseier, R.: Sea ice validation, in: DMSP Special Sensor Microwave/Imager Calibration/Validation, 1991.

Rothrock, D. A., Thomas, D. R., and Thorndke, A. S.: Principal component analysis of satellite passive microwave data over sea ice, Journal of Geophysical Research: Oceans, 93, 2321–2332, doi:10.1029/JC093iC03p02321, 1988.

SEARCH: Research, Synthesis, and Knowledge Transfer in a Changing Arctic: The Study of Environmental Arctic Change (SEARCH), Tech. rep., Arctic Research Consortium of the United States, 2013.

Shokr, M. and Sinha, N.: Sea Ice. Physics and Remote Sensing, AGU- WILEY, 2015.

Shokr, M., Lambe, A., and Agnew, T.: A new algorithm (ECICE) to estimate ice concentration from remote sensing observations: an application to 85-GHz passive microwave data, IEEE T. Geosci. Remote, 46, 4104–4121, 2008.

Smith, D.: Extraction of winter total sea-ice concentration in the Greenland and Barents Seas from SSM/I data, Int. J. Remote Sens, 17, 2625–2646, 1996.

Stroeve, J., Serreze, M., Holland, M., Kay, J., Malanik, J., and Barrett, A.: The Arctic's rapidly shrinking sea ice cover: a research synthesis, Climatic Change, 110, 1005–1027, doi:10.1007/s10584-011-0101-1, 2012.

Talone, M., Portabella, M., Martínez, J., and González-Gambau, V.: About the Optimal Grid for SMOS Level 1C and Level 2 Products, IEEE Geoscience and Remote Sensing Letters, 12, 1630–1634, doi:10.1109/LGRS.2015.2416920, 2015.

Thomas, D. and Dieckmann, G., eds.: Sea Ice. An Introduction o its physics, Chemistry, Biology and geology, Blackwell, 2003.

Tiuri, M., Sihvola, A., Nyfors, E., and Hallikaiken, M.: The complex dielectric constant of snow at microwave frequencies, IEEE Journal of Oceanic Engineering, 9, 377–382, doi:10.1109/JOE.1984.1145645, 1984.

Tonboe, R. T., Eastwood, S., Lavergne, T., Sørensen, A. M., Rathmann, N., Dybkjær, G., Toudal Pedersen, L., Høyer, J. L., and Kern, S.: The EUMETSAT sea ice climate record, The Cryosphere Discussions, 2016, 1–39, doi:10.5194/tc-2016-34, http://www.the-cryosphere-discuss.net/tc-2016-34/, 2016.

Ulaby, F. and Long, D.: Microwave Radar adn Radiometric Remote Sensing., University of Michigan Press, 2014.

Ulaby, F., Moore, R., and Fung, A.: Microwave Remote Sensing. Active and Passive., Addison-Wesley Publishing Company. Advanced Book Program/World Science Division., 1986.

Vant, M., Ramseier, R., and Makios, V.: he complex-dielectric constant of sea ice at frequencies in the range 0.1–40 GHz, T J. Appl. Phys., 49, 1264–1280, 1978.

Vihma, T.: Effects of Arctic Sea Ice Decline on Weather and Climate: A Review, Surveys in Geophysics, 35, 1175–1214, doi:10.1007/s10712-014-9284-0, 2014.

Wilheit, T. T.: A review of applications of microwave radiometry to oceanography, Boundary-Layer Meteorology, 13, 277–293, doi:10.1007/BF00913878, 1978.

Zine, S., Boutin, J., Font, J., Reul, N., Waldteufel, P., Gabarro, C., Tenerelli, J., Petitcolin, F., Vergely, J., Talone, M., and Delwart, S.: Overview of the SMOS Sea Surface Salinity Prototype Processor, IEEE Transactions on Geoscience and Remote Sensing, doi:10.1109/TGRS.2008.915543, 2008.

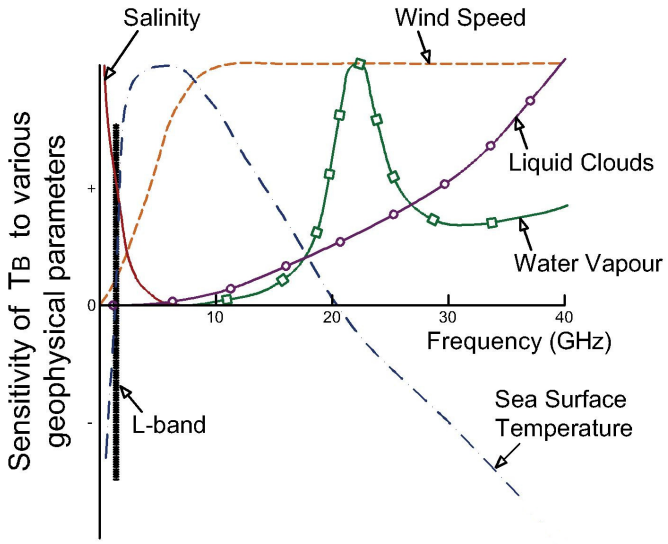

Figure 1. Sensitivity of brightness temperature for open seawater over a range of observing frequencies in the microwave band for a set of key geophysical parameters (created after Wilheit (1978) and Ulaby and Long (2014)). The maximum sensitivity of T_B to sea surface temperature is around 6 GHz, with a peak of 0.4 $K/^\circ C$; to salinity is around 1 GHz, with a peak value of 0.5 K/psu; to wind speed is above 10 GHz, with a peak value of 1 K/m/s. The peak of attenuation from water vapor in clouds is at 22 GHz, and is 0.2 DB/km. L-band (1.4 GHz) observations are hardly sensitive to any variable but salinity, hence it is in a sweet spot for sea ice studies.

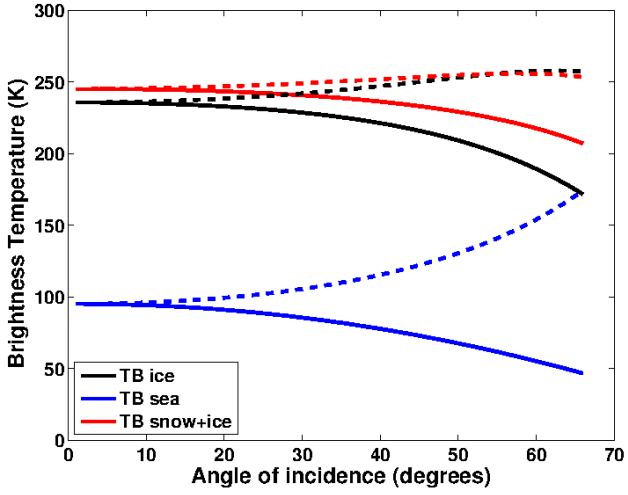

Figure 2. Theoretical variation of brightness temperature with angle of incidence for (blue) seawater, (black) sea ice, and (red) a snow layer overlying a sea ice layer for (continuous) horizontal and (dashed) vertical polarizations. (See text in Sect. 3 for details.)

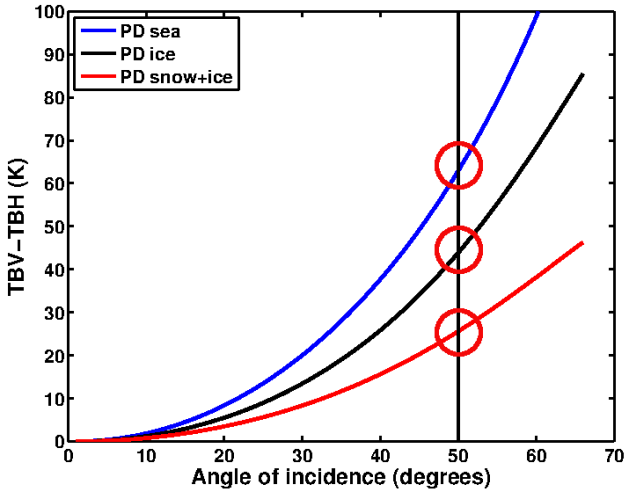

Figure 3. Modeled variation of polarization difference (PD) index with angle of incidence for (blue) seawater, (black) sea ice, and (red) a snow layer overlying a sea ice layer. (See Eq. 8 and text in Sec. 4.1 for details.) The vertical line at 50° incidence angle is drawn for reference to tie points, which are marked with a solid circle for the three media (see text in Sec. 4.2).

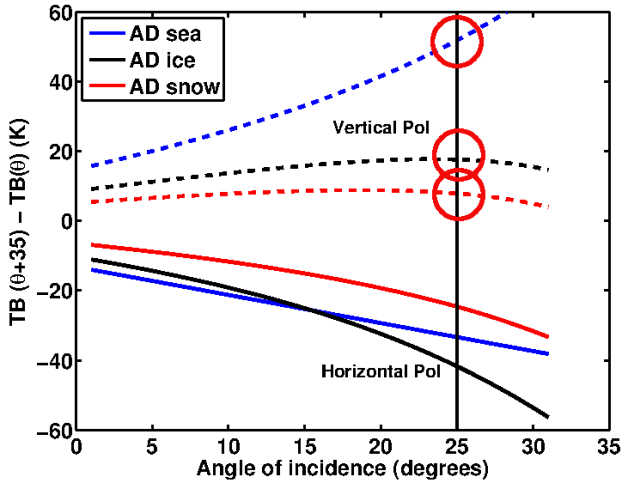

Figure 4. Modeled variation of angular difference index (AD) with angle of incidence for (blue) seawater, (gray) sea ice, and (red) a snow layer overlying a sea ice layer for (continuous) horizontal and (dashed) vertical polarizations, and for $\Delta\theta = 35^\circ$. (See Eq. 9 and text in Sec. 4.1 for details.) The vertical line at 25° incidence angle is drawn for reference to tie points, which are marked with a solid circle on vertical polarization for the three media (see text in Sec. 4.2).

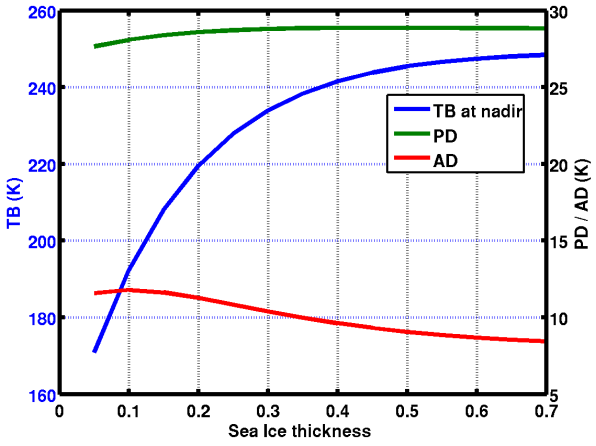

Figure 5. Theoretical variation with sea ice thickness of (blue; left axis) T_B at nadir, (green; right axis) polarization difference (PD) at 50° incidence angle, and (red; right axis) angular difference (AD) at $\Delta\theta = 25^\circ$ after the model by Burke et al. (1979), for a sea ice salinity of 8 psu, sea ice temperature of -10° C, and a snow layer of 10-cm thick over the ice. (See text in Sect. 3 for details.) Note the factor of 10 change between the left/right vertical scales.

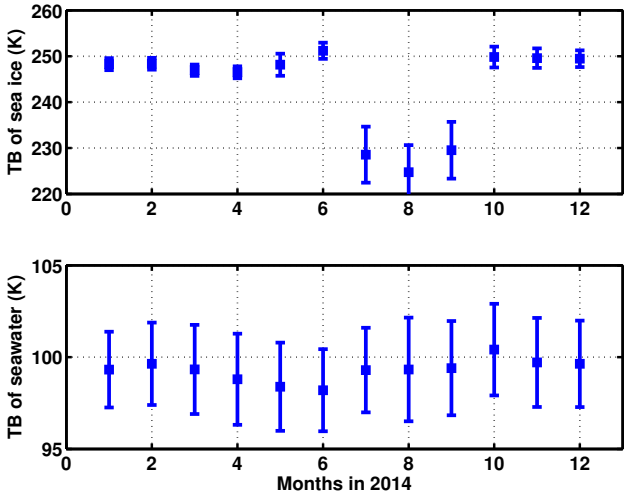

Figure 6. Temporal variation of the average brightness temperature T_B at nadir for (top) sea ice and (bottom) seawater at the two tie-point regions (see Sec. 4.4). Note the factor of 4 change in the vertical scales.

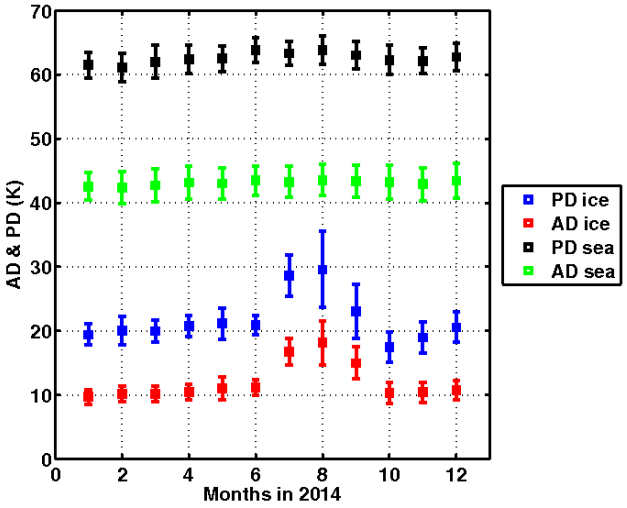

Figure 7. Same as Fig. 6 except here for angular and polarization difference indices.

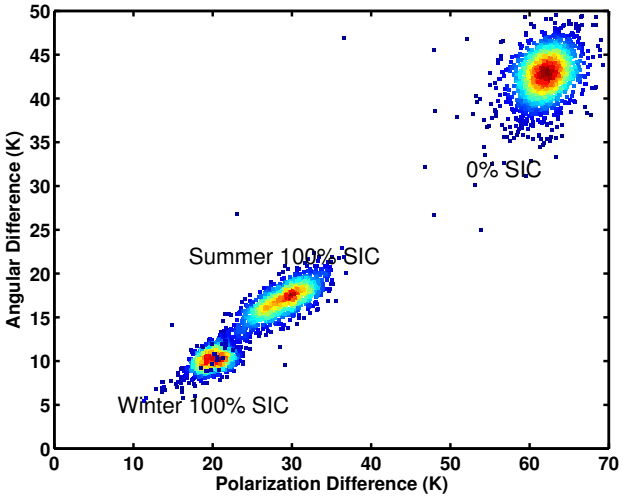

Figure 8. Scatter plot of the angular difference vs polarization difference in March and July 2014, with (red-to-blue) high-to-low index occurrence values for the two tie-point regions, i.e., 0% and 100% sea ice concentration (SIC).

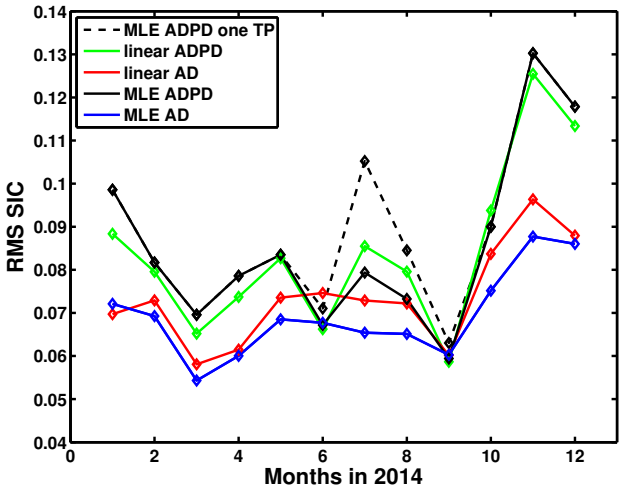

Figure 9. Comparison of one tie-point (black dotted line) vs two tie-points (black plane line) with MLE; and MLE vs linear retrieval tecniques. If not defined in the labels is tie-points.

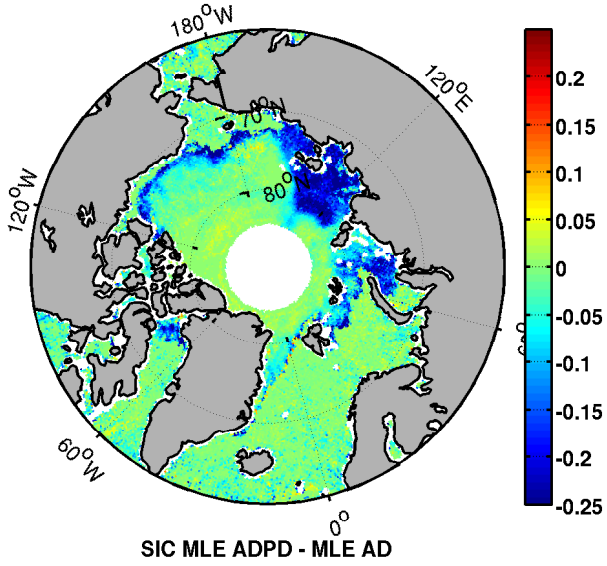

Figure 10. SMOS SIC with MLE AD+PD minus SMOS SIC with MLE AD inversion tecniques.

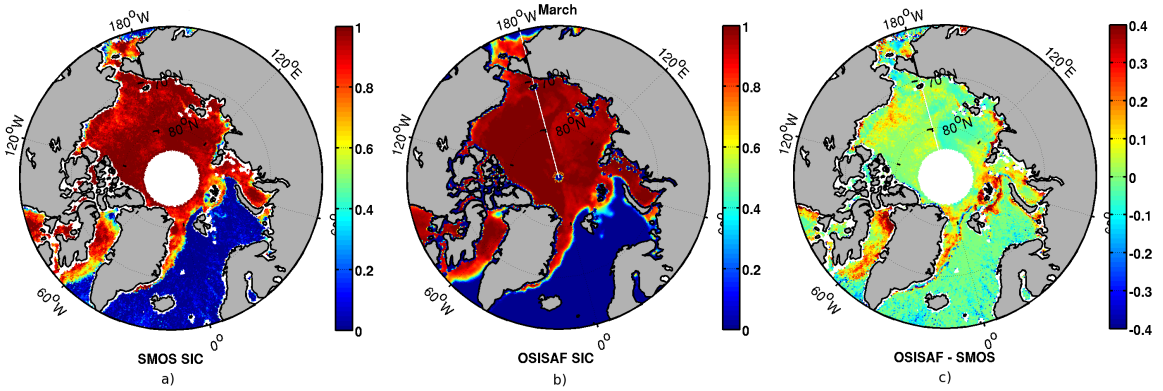

Figure 11. SMOS SIC with MLE (a), OSISAF SIC (b) and the differences (c) for 3th March 2014.

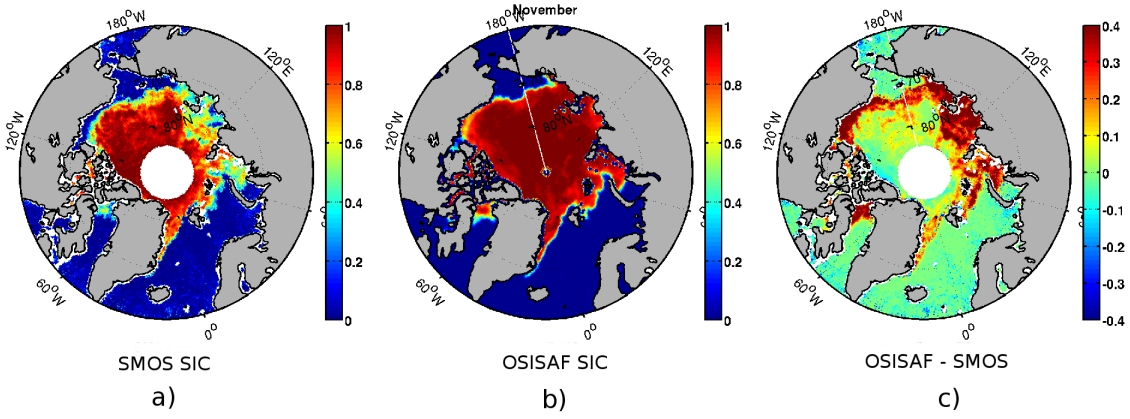

Figure 12. SMOS SIC with MLE (a), OSISAF SIC (b) and the differences (c) for 3th November 2014.

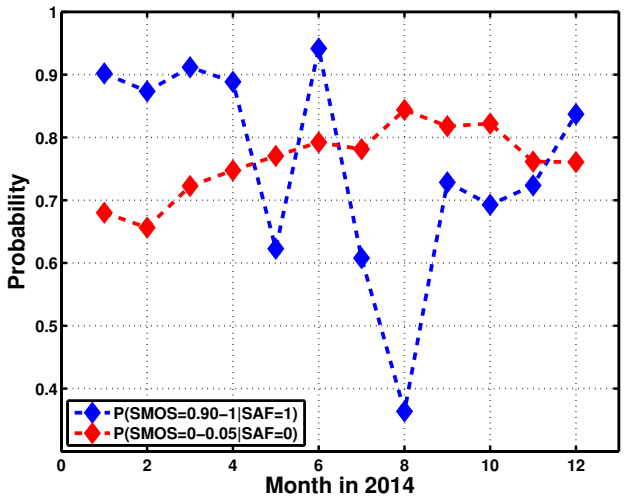

Figure 13. Probability to have SMOS SIC more than 0.90 where OSISAF SIC=1 (blue line) and SMOS SIC less than 0.05 where OSISAF SIC=0 (red line) for 2014. Summer tie points are used for retrievals from June to September.

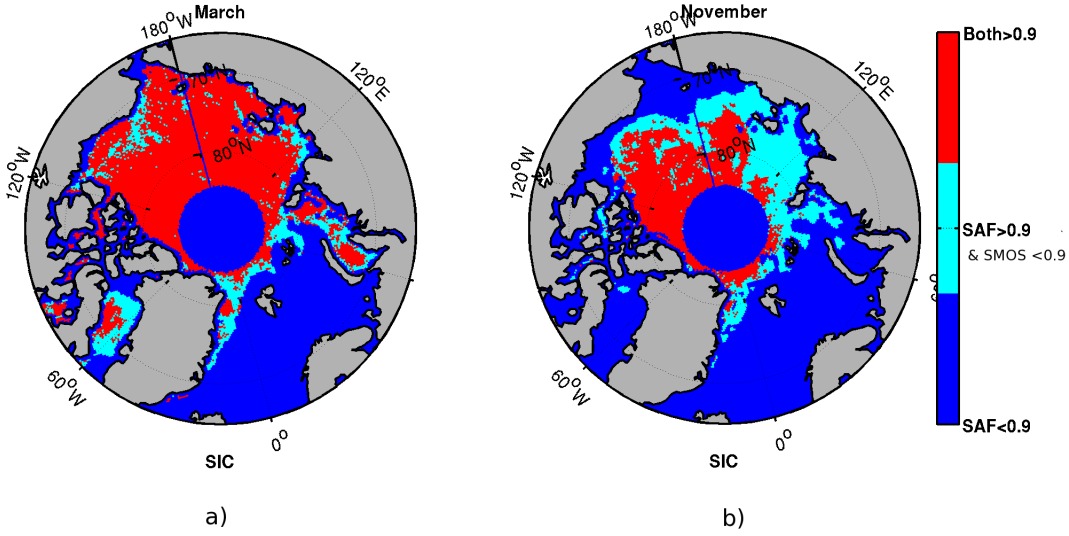

Figure 14. Classification of the Artic region according to their values of SMOS and OSI-SAF SIC during March (a) and November (b) 2014. Three classes are shown: 1) OSISAF $SIC < 0.9$; 2) OSISAF $SIC > 0.9$ and SMOS $SIC < 0.9$; and 3) OSISAF $SIC > 0.9$ and SMOS $SIC > 0.9$.

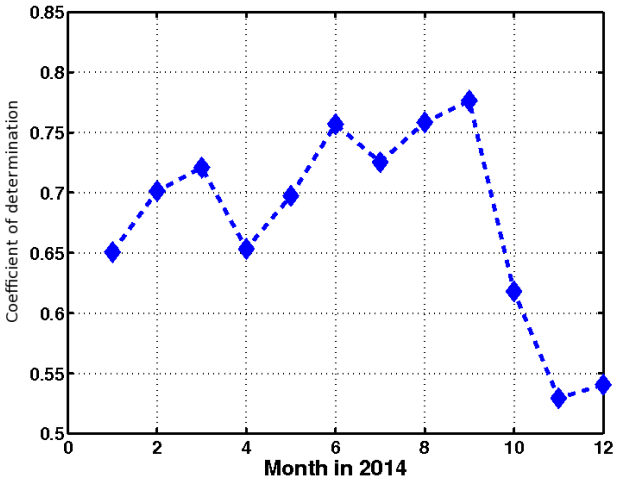

Figure 15. Coefficient of determination (R^2) between SMOS and OSISAF SIC for 2014, considering only SIC data in the range from 5% to 95%.

Table 1. Modeled (with and without snow) and SMOS observed T_B, PD, and AD median values. Errors quoted are the standard deviation around the median.

		Modeled (K)		Observed all year median $\pm\sigma$ (K)	
0% SIC (Seawater)	T_B	95.2		99.33 ± 2.40	
	PD	62.9		62.56 ± 2.56	
	AD	51.8		43.08 ± 2.57	
		Modeled with snow (K)	Modeled without snow (K)	Observed Winter median $\pm\sigma$ (K)	Observed Summer median $\pm\sigma$ (K)
100% SIC (Sea Ice)	T_B	249.2	239.3	248.21 ± 1.56	229.04 ± 4.99
	PD	26.8	45.9	20.30 ± 1.75	25.53 ± 3.72
	AD	8.6	18.8	10.38 ± 1.17	15.26 ± 2.31

Table 2. Sensitivity of measurement T_B, PD, and AD to ice temperature (T), salinity (S), and thickness (d).

Medium	Index (I)	$\delta I/\delta T$ (K /° C)	$\delta I/\delta S$ (K / psu)[1]	$\delta I/\delta d$ (K / cm)
Seawater	T_B	0.2	0.51	
	PD	0.26	0.21	
	AD	0.20	0.12	
Sea ice	T_B	0.85	1.00	1.2
	PD	0.66	0.35	0.02
	AD	0.35	0.25	0.05

[1] practical salinity units

Table 3. Propagated SIC error using each index, computed from Eq. 10 for assumed (T, S, d) variations, and root-sum-squared (RSS).

SIC error (%)	index used	ΔT 5 K	ΔS 4 psu	Δd 30 cm	RSS
ΔSIC	TB	2.8	2.6	23.4	23.7
ΔSIC	PD	7.6	3.2	1.4	8.3
ΔSIC	AD	4.8	2.8	4.2	7.0